Constraints on Flow Regimes in Wide-Aperture Fractures

Teamrat A.Ghezzehei

Earth Sciences Division
Lawrence Berkeley National Laboratory
University of California
MS 90R1116, 1 Cyclotron Road
Berkeley, California 94720-8126

Tel 510-486-5688
Fax 510-486-5686
Email TAGhezzehei@lbl.gov

Manuscript in preparation to be submitted to
Water Resources Research

NOTES

Last Edited: January 22, 2004

File: F:\Current Projects\08 Instability\Constrains for wide fractures REVB.doc

Citation Library: F:\Bibliographic\References\master.enl

Abstract

In recent years, significant advances have been made in our understanding of the complex flow processes in individual fractures, aided by flow visualization experiments and conceptual modeling efforts. These advances have led to the recognition of several flow regimes in individual fractures subjected to different initial and boundary conditions. Of these, the most important regimes are film flow, rivulet flow, and sliding of droplets. The existence of such significantly dissimilar flow regimes has been a major hindrance in the development of self-consistent conceptual models of flow for single fractures that encompass all the flow regimes. The objective of this study is to delineate the existence of the different flow regimes in individual fractures. For steady-state flow conditions, we developed physical constraints on the different flow regimes that satisfy minimum energy configurations, which enabled us to segregate the wide range of fracture transmissivity (volumetric flow rate per fracture width) into several flow regimes. These are, in increasing order of flow rate, flow of adsorbed films, flow of sliding drops, rivulet flow, stable film flow, and unstable (turbulent) film flow. The scope of this study is limited to wide-aperture fractures with the flow on the opposing sides of fracture being independent.

1. Introduction

The development of realistic and robust predictive models of flow and transport in fractured geologic media requires a thorough understanding of the physical processes that govern flow in individual fractures. In recent years, significant advances have been made in our knowledge of these complex processes, aided by flow visualization experiments and conceptual modeling of single-fracture flows [e.g., *Amundsen et al.*, 1999; *Bertels et al.*, 2001; *Detwiler et al.*, 2002; *Dobson et al.*, 2003; *Doe*, 2001; *Dragila*, 1999; *Fourar et al.*, 1993; *Glass and Nicholl*, 1996; *Glass et al.*, 2002; *Kneafsey and Pruess*, 1998; *Nicholl et al.*, 1994; *Or and Tuller*, 2000; *Persoff and Pruess*, 1995; *Su et al.*, 2001; *Su et al.*, 1999; *Tokunaga and Wan*, 1997; *Tokunaga et al.*, 2000; *Zhong et al.*, 2001]. One important outcome of these endeavors is the recognition that several flow regimes exist in individual fractures that are subjected to different initial and boundary conditions.

The simplest flow regime, both physically and mathematically, involves a stable and flat film of liquid that lines the entire surface of planar and smooth fractures. Using laboratory flow experiments, *Tokunaga and Wan* [1997] demonstrated that film flow is a very important mechanism of flow in unsaturated fractured media. Their findings were followed by a surge of interest in the role of films in vadose zone processes [e.g., *Amundsen et al.*, 1999; *Berkowitz*, 2002; *Bertels et al.*, 2001; *Kneafsey and Pruess*, 1998; *Or and Tuller*, 2000; *Pruess*, 1999; *Tokunaga and Wan*, 2001; *Tokunaga et al.*, 2000]. Such flat films are inherently unstable. At high flow rates, capillary forces and/or inertia create waves (ripples) that travel on the film surface [*Berbente and Ruckenst*, 1968; *Brauner*, 1989; *Jayanti and Hewitt*, 1997; *Lee*, 1969; *Patnaik and Perez-Blanco*, 1996; *Penev et al.*, 1972; *Soo*, 1996; *Yih*, 1963]. These surface waves can be responsible for enhanced travel velocity and transport in unsaturated fractures, which

cannot be explained by stable film flow alone [*Dragila*, 1999; *Dragila and Wheatcraft*, 2001]. On the other hand, at lower flow rates, the films disintegrate into thin threads or rivulets [*Bankoff*, 1983; *El-Genk and Saber*, 2001; *Hughes and Bott*, 1998; *Joo et al.*, 1996]. Similar formation of rivulets in narrow-aperture fractures was observed by *Su et al.* [1999] and *Su et al.* [2001]. At even lower flow rates, the threads and rivulets break up into trains of sliding drops [*Schmuki and Laso*, 1990] and blobs [*Su et al.*, 2001; *Su et al.*, 1999]. *Doe* [2001] contends that these sliding drops could play an important role in the unstable flow phenomena observed in fractured media. At extremely low flow rates, flow in fractures is carried by thin adsorbed films, on the order of a few molecular layers [*Or and Tuller*, 2000; *Tuller et al.*, 1999].

The existence of such significantly dissimilar flow regimes poses a major challenge in the pursuit of a unified, self-consistent conceptual model of flow for a single fracture and a network of fractures. The problem is apparent in most numerical simulators, which lack adequate and unified representation of the various flow regimes. In fact, the Committee on Fracture Characterization and Fluid Flow of the *National Academy of Sciences* [1996] concluded that "most of the error involved in predicting flow behavior [in rock fractures] with a numerical model is usually due to deficiencies in the underlying conceptual models." For example, the consequences of assuming fully wetting film flow (when in fact, the flow is occurring in rivulets) could mean a gross overestimation of contaminant travel time and/or diffusion into matrix [see Table 1 of *Dragila and Weisbrod*, 2003].

The lack of full understanding of the constraints on the potential flow regimes, and the transitions between them, is a critical hurdle in integrating the flow regimes into a unified conceptual model. The mathematical expressions devised to model certain flow regimes (e.g., stable films, rivulets) are often used without sufficient constraints concerning the physical

existence of the assumed regime. As a result, models of competing flow regimes are expected to yield vastly different results for identical boundary and initial conditions.

The foregoing discussions assert the need for a common set of criteria by which all potential flow regimes can be tested and compared, thereby enabling identification of the most likely regime for a given set of flow conditions. The objective of this study was to set physical constraints for some common flow regimes, by seeking the regime that satisfies a minimum energy configuration. By focusing on the steady state pictures alone, we were able to derive analytical and semi-analytical expressions for the bounds of the different flow regimes.

2. Fracture and Liquid Properties

Perhaps the most challenging aspect of modeling flow in fractured media is characterization of individual fractures and fracture networks. Within a single fracture, numerous features of the fracture have strong bearing on the prevalent flow processes; these include roughness, inclination, aperture, and matedness [*Hakami and Larsson*, 1996]. A standard system of representation for these geometric features is yet to be developed. On the other hand, the physical properties of the flowing liquid are rather constant. If needed, changes in these properties due to variations in chemistry, temperature, or pressure are straightforward to account for. The single most important parameter that describes the interaction between fracture surfaces and the flowing liquid is the contact angle. In the following two subsections, we outline sets of simplifying assumptions regarding the fracture geometry and contact angle. In this section, we look at (1) fracture-surface properties, (2) liquid properties, and (3) the interaction between the fracture and liquid.

2.1. Fracture Geometry

We chose a simple fracture geometry that enables us to explore flow behaviors over a wide range of flow rates. The important features of this simple geometry are:

1. The fracture is smooth enough with negligible effects on the liquid flow.

2. The fracture aperture (opening) is large enough for the flows along the two faces of the fracture to be considered independent.

3. The fracture surface is planar, and a single inclination angle suffices to describe the gravitational head gradient.

2.2. Intrinsic and Apparent Contact Angles

The contact angle that a liquid drop at rest makes with a substrate is a manifestation of the balance between cohesive and adhesive forces. The equilibrium (intrinsic) contact angle of a liquid on clean and molecularly smooth surfaces (e.g., surface of mineral grains) is a function of the interplay between the solid-liquid, solid-vapor, and liquid-vapor interfacial energies as given by Young's equation

$$\cos\theta = \frac{\sigma_{SV} - \sigma_{SL}}{\sigma_{LV}} \tag{1}$$

where σ is the surface free-energy (surface tension), and the subscripts L, S, and V denote liquid, solid, and vapor, respectively. Most natural surfaces including fracture faces are neither clean nor smooth, and the solid-liquid and solid-vapor interfacial energies are not uniform throughout the surfaces. Therefore, the apparent contact angle a liquid makes with a chemically and/or geometrically heterogeneous surface is deemed different from the intrinsic values. The effect of heterogeneity on contact angle is discussed in depth by *Adamson and Gast* [1997]. The

apparent contact angle (θ_0) a liquid makes with a chemically homogenous surface but with geometric features that resemble a screen (or woven material) is described by Cassie's law [*Cassie,* 1948],

$$\cos\theta_0 = (1-\varphi)\cos\theta - \varphi \tag{2}$$

where φ is the fraction of the surface occupied by local maxima (e.g., tips of microcrystals), which can be considered as a measure of the microroughness. In general, Cassie's law implies that the apparent contact angle is usually larger than the intrinsic value and that the enhancement of the apparent contact angle over the intrinsic value increases with openness (fewer maxima) of the microroughness. Natural evidence of this concept is apparent on the hydrophobicity of duck's back ($\theta_0 \approx 150°$) because the interlocking barbules (with intrinsic contact angle of $\theta_0 \approx 100°$) create microroughness with $\varphi \approx 0.5$ [*Adamson and Gast,* 1997]. Without going into the details of measuring fracture surface microroughness, we assume that θ_0 is an experimentally measurable quantity. Most of the illustrative calculations shown in this paper use an apparent contact angle of $\theta_0 = 20°$. In the summary (section 6), the role of a wider range of contact angles ($0° \le \theta_0 \le 90°$) is shown.

3. Flow Equations

The main objective of this study is to set constraints on the steady-state flow rate so as to delineate the existence of various flow regimes. Transient phenomena, such as fingering of a wetting front as a liquid invades a dry fracture, are not considered. However, we do not preclude inherently unstable flow regimes (such as intermittent rivulet snapping) that occur under globally steady-state flow conditions. Moreover, we are not concerned with the full detail of the transition from one regime to another that arises because of changes in boundary conditions.

Photographs of flow visualization experiments conducted by *Schmuki and Laso* [1990] (shown in Figure 1) are used to explain the classification of flow regimes employed in this paper. In these experiments, liquid was delivered to the upper edge of an inclined smooth surface at a steady flow rate using narrow tubing. Figure 1 shows snapshots taken at different flow rates. At the highest flow rate in the experiments, *Schmuki and Laso* [1990] observed a wide falling "film" with wavy surface (Figure 1a). A decrease in flow rate resulted in meandering rivulet, which bifurcated into multiple smaller rivulets (Figure 1b). Further decrease in flow rate resulted in "straight rivulets" as shown in Figure 1c. At the lowest flow rate (Figure 1a), a train of equally spaced "sliding drops" was formed.

Figure 1. Photos of different flow regimes from experiments conducted by Schmuki and Laso [1990] (a) wavy film flow, (b) meandering rivulets, (c) straight rivulet, and (d) sliding drops. (Permission to reprint will be requested).

3.1. Conceptual Models

The observations of *Schmuki and Laso* [1990] lead us to recognize at least three distinct flow regimes that are likely to occur in unsaturated fractures. These are, from the highest flow rate to the lowest, falling film flow, rivulet flow, and sliding-drop flow. These flow regimes are schematically illustrated in Figure 2 and briefly defined below.

Figure 2. Conceptual geometries of flow regimes used in this study.

Falling film flow is defined as a complete wetting of the fracture surface by a sheet of liquid (Figure 2a). The importance of films in flow through fractured rocks was demonstrated by laboratory experiments of *Tokunaga and Wan* [1997]. Note that this type of hydrodynamic film is much thicker and significantly different from adsorbed films that are on the orders of a few to

several molecular layers [see e.g., *Or and Tuller*, 2000; *Tuller et al.*, 1999 for the role of adsorbed films on flow and transport in porous media]. For the most part of this study, we consider laminar flow conditions with uniform film thickness that is directly proportional to the flow velocity. At very high flow rates, these assumptions are invalid because such films are susceptible to waviness and instabilities arising from local surface tension differences and/or dominance of inertial forces. The waves usually travel at much faster velocities than the average film substrate and their description is expected to account for the episodicity that arises as a result of the fast waves [*Dragila*, 1999; *Dragila and Wheatcraft*, 2001]. An upper limit to the stable film flow regime is provided in subsection 5.5 based on the Reynolds number.

As the flow rate is reduced, the stable film disintegrates into slender threads or rivulets. Rivulet flow typically involves equidistant and identical threads of liquid with uniform cross section, as shown in Figure 2b. Rivulet flow is often observed on walls of shower rooms or automobile windshields, or as streaks of rain on concrete walls [see *Benson*, 2001 for the latter example]. In this study, we consider fully developed laminar rivulets, ignoring the detailed dynamics of finger formation at the boundaries of stable films. In subsection 5.4, the boundary between film flow regime and rivulet regime is derived based on minimum-energy configurations.

With further decrease in flow rate, the rivulets break up into sliding droplets. Sliding drops occur for example, when small quantity of liquid is sprayed on a solid surface (shower sprays on walls and rain drizzles on windshields). The potential importance of sliding drops for flow in fractures in the vadose zone was discussed in detail by *Doe* [2001].

In the following subsections, simplified geometries and flow equations of the flow regimes described above are introduced. A Cartesian coordinate system with the flow rate

aligned parallel to the z-axis is used, as shown in Figure 2. In all the cases, the system is assumed to be isothermal, and the wetting fluid is considered incompressible with constant Newtonian-viscosity μ and density ρ. A passive non-wetting fluid (e.g., air in an air-water system) is considered. Fluid flow is driven by the gravitational potential gradient,

$$\Xi = \rho \cdot g \cdot \cos(\alpha) \tag{3}$$

where α is the fracture inclination angle measured from the vertical. The liquid flow on the fracture surface is described by the equations of momentum conservation and continuity

$$\nabla^2 u - \beta = 0 \tag{4}$$

where u is the liquid velocity and $\beta = \Xi/\mu$. We consider a constant volumetric flow rate of Q applied uniformly across a fracture with transverse width of W.

3.2. Falling Film Flow

The profile of a falling film (in the direction of flow) is assumed to be of uniform thickness, as shown in Figure 3. The thickness of such stable and flat films is commonly referred to as "Nusselt film thickness" [e.g., see *Dragila*, 1999, page 48]. Assuming the flow is fully developed and laminar, the steady-state solution to the flow equation (4) yields a velocity profile given by

$$u_f(y) = \beta\left(h_f\, y - \frac{y^2}{2}\right) \tag{5}$$

where h_f is the film thickness. The total volumetric flow rate is defined as the product of the average velocity (obtained by integrating the film velocity (5) along the film thickness) and film cross-sectional area ($h_f \times W$),

193 $$Q = W\, h_f \int_0^{h_f} u_f \, \mathrm{d}\, y = W\, \beta \frac{{h_f}^3}{3} \tag{6}$$

194 By rearranging (6), the film thickness can be expressed as a function of the flow rate, Q,

195 $$h_f = \left(\frac{3\, q}{\beta} \right)^{1/3} \tag{7}$$

196 where $q = Q/W$ is defined as transmissivity of the fracture.

197 Figure 3. Schematic representation of a falling film and its velocity profile.

198 **3.3. Rivulet Flow**

199 We employ two approximations regarding the rivulet geometry and the velocity profile to
200 facilitate the derivation of analytical expressions for the total system energy (see section 4). First,
201 we assume that the capillary pressure is uniform throughout the cross section of the rivulet
202 [*Mikielewicz and Moszynski*, 1976]. This assumption implies that the rivulet cross section can be
203 represented by a circular arc of radius R_r, as illustrated in Figure 4 [*Bankoff*, 1971]. Then, the
204 liquid-vapor interface is parametrically given by

205 $$h_r(x) = R_r \left(\cos\gamma - \cos\theta_0 \right) \tag{8}$$

206 where h_r is the rivulet height at a distance x from the axis of the rivulet ($x = R_r \sin\gamma$) and the
207 polar subtended angle is $0 \le \gamma \le \theta_0$.

208 Figure 4. Schematic representation of the cross-section of a straight rivulet.

209 Secondly, we consider zero-order approximation of the fluid velocity such that an
210 infinitesimal slice of the rivulet, with a width of $\mathrm{d}\, x$, behaves as a uniform falling film [*Bankoff*,

211 1971; *Towell and Rothfeld*, 1966]. Then substituting (8) for the Nusselt film thickness, h_f, in (5)

212 leads to

213 $$u_r(x,y) = \beta \cdot \left(h_r(x) y - \frac{y^2}{2} \right) \tag{9}$$

214 *Allen and Biggin* [1974] showed that the approximate solution (9) matches reasonably

215 well with the finite element solution of (4) except in the neighborhood of the edges. As the

216 contact angle approaches $\pi/2$, the zero-order approximation fails because the slope of the liquid-

217 vapor interface grows rapidly near the edges.

218 Considering that there are n_r identical rivulets across a fracture of width W, the total

219 flow rate of all the rivulets is given by,

220 $$Q = n_r \int_{-w_r/2}^{w_r/2} \int_0^{h(x)} u_r(x,y)\,\mathrm{d}y\,\mathrm{d}x = \frac{2 n_r}{3} \beta R^4 f_1(\theta_0) \tag{10}$$

221 where the rivulet width is

222 $$w_r = 2 R_r \sin\theta_0 \tag{11}$$

223 and the function $f_1(\theta_0)$ is given by,

224 $$\begin{aligned} f_1(\theta_0) &= \int_0^{\theta_0} \cos\theta \left(\cos\theta - \cos\theta_0\right)^3 d\theta \\ &= \frac{36\theta_0 + 24\theta_0 \cos 2\theta_0 - 28 \sin 2\theta_0 - \sin 4\theta_0}{32} \end{aligned} \tag{12}$$

225 By rearranging (10) the rivulet radius can be expressed as a function of the flux

226 $$R_r = \left(\frac{3q}{2 (n_r/W) \beta f_1(\theta_0)} \right)^{1/4} \tag{13}$$

227 The fraction of the fracture width not wetted by the flowing rivulets is given as

228 $$\frac{d_r}{W} = 1 - \frac{n_r}{W} w_r = 1 - 2\frac{n_r}{W} R_r \sin\theta_0 \qquad (14)$$

229 Strictly speaking, the dry space may be lined with very thin layer of adsorbed film [*Tuller*
230 *et al.*, 1999]; nevertheless, its contribution compared to the rivulet flow is negligible.

231 **3.4. Sliding drops**

232 The importance of sliding drops to flow in unsaturated fractures was recently highlighted
233 by *Doe* [2001]. Compared to the preceding two flow regimes, the mathematics of sliding drops is
234 far more complicated. Unlike the rivulet thickness or rivulet radius, which are functions of only
235 the flow rate and the contact angle, the geometry of sliding drops involves a free surface whose
236 configuration is non-linearly dependent upon the volume and velocity. Because of this
237 complexity, there are only a few studies that have attempted to describe the problem of sliding
238 drops based on first principles. Recently, *Podgorski et al.* [2001] showed that small drops sliding
239 down a slightly hydrophobic surface assume different shapes depending on their capillary
240 number,

241 $$Ca = \mu v_d / \sigma_{LV} \qquad (15)$$

242 where v_d is the velocity of the drop. Without going into a detailed description of the three-
243 dimensional flow field and exact geometry of the associated free-surface, *Podgorski et al.* [2001]
244 derived a force-balance based scaling law relating the drop volume to the sliding velocity that
245 takes into consideration that:

246 1. The drop velocity (v_d) is governed by the in-plane component of its weight $\rho g V_d \cos\alpha$,
247 where V_d is the drop volume;

248 2. A typical viscous drag of order $\mu v_d V_d^{1/3}$ resists the sliding velocity; and

3. A capillary force induced by of the nonuniformity of the contact angle along the perimeter of the drop resists the weight. This resistance scales as $\Delta\theta\,\sigma_{LV}\,V_d^{1/3}$, where $\Delta\theta$ is a perimeter-averaged projection factor of surface tension.

Figure 5. Definition of variables representing a sliding drop.

The scaling law is written in terms of non-dimensional numbers as

$$Ca = \gamma\, Bo \cos\alpha - \Delta\theta \tag{16}$$

where $Bo = V^{2/3}\rho\, g/\sigma_{LV}$ is the Bond number and γ is a proportionality constant. *Podgorski et al.* [2001] compared (16) with data from experiments using silicone-oil droplets on surfaces coated with fluoro-polymer. Their plots suggest that γ and $\Delta\theta$ are almost identical for the rounded and cornered drop shapes. However, the cusped drops have significantly higher γ and $\Delta\theta$ values. In the above scaling law γ and $\Delta\theta$ are empirical constants that depend on the fluid and solid properties. For subsequent analyses we estimate these constants from experimental data of *Kim et al.* [2002] who determined the sliding velocity of drops with known volume on smooth polycarbonate planes inclined at different angles. We plotted their data in terms of the dimensionless numbers (see Figure 6) and fitted (16) to the data. The properties of the liquids used in the experiments and the best-fit γ and $\Delta\theta$ values are listed in Table 1. The data in Table 1 suggest that the fitted γ and $\Delta\theta$ are weakly related to viscosity, but both seem to increase with surface tension. Because the surface tension of glycerin is the closest to that of water, in subsequent illustrative calculations the values of γ and $\Delta\theta$ corresponding to glycerin are considered as representative of water on rock surface.

Figure 6. Relationship between Capillary number and Bond number for sliding drops of different liquids on smooth polycarbonate surface [*Kim et al.*, 2002] and fitted scaling law given by (16).

Small drops, whose characteristic size (radius) is smaller than the capillary number, have spherical-cap shape on a horizontal plane. For simplicity, we ignore the distortion from this ideal geometry and assume the drop shape is a spherical cap at all times as shown in Figure 5. The radius of the equivalent spherical drop is related to the drop volume by

$$R_d = V_d^{1/3}\left\{\frac{3}{4\pi\sin^4(\theta_0/2)(2+\cos\theta_0)}\right\}^{1/3} \tag{17}$$

The sliding velocity of the drop is related to the drop volume according to (16), which can be rearranged as

$$v_d = \gamma\beta V_d^{2/3} - \frac{\sigma_{LV}}{\mu}\Delta\theta \tag{18}$$

Consider there are n_d drop paths per width W and that the number of drops in the train of drops in a fracture of length L is m_d, as illustrated in Figure 2c. The time it takes for an individual drop to traverse the axial inter-drop separation distance $x_d = L/m_d$ is $t_d = x_d/v_d$. Then, the total volumetric flux traversing an arbitrary line normal to the flow direction is given by

$$q = \frac{n_d}{W}\frac{V_d}{t_d} = \frac{n_d\ m_d}{L} V_d\ v_d \tag{19}$$

Upon substitution of (18) in (19) we arrive at

$$q = \frac{n_d}{W}\frac{m_d}{L} V_d \left(\gamma\beta V_d^{2/3} - \frac{\sigma_{LV}}{\mu}\Delta\theta\right) \tag{20}$$

Equation (20) cannot be solved for V_d in closed-form.

289 Table 1. Properties of liquids used by [*Kim et al.*, 2002] and fitted empirical
290 constants

291 4. Energy Equations

292 As pointed out in the introduction, the main goal of this paper is to identify the most
293 likely flow regime for a given flow condition (flow rate, fluid type, and fracture properties). The
294 approach we use to discern the most stable flow regime for a given flow condition is that of
295 "minimum energy configuration". The concept of minimum energy configuration has been used
296 to estimate the minimum film thickness before it breaks up into rivulets [*Hobler*, 1964]. The
297 method has been refined and used to study film and rivulet flows on flat surfaces, and inside and
298 outside surfaces of pipes [*Bankoff*, 1971; *El-Genk and Saber*, 2001; *Mikielewicz and Moszynski*,
299 1976; *Ponter and Aswald*, 1977; *Schmuki and Laso*, 1990].

300 The concept of minimum energy configuration states that the configuration with the
301 lowest total energy (sum of kinetic and interfacial potential energies) per unit width of fracture
302 has the highest likelihood of occurrence. Mathematically, the total system energy is given by

303 $$E_T = \frac{\rho}{2}\iint_{A_L} u^2 dx\,\mathrm{d}\,y + A_{SL}\sigma_{SL} + A_{SV}\sigma_{SV} + A_{LV}\sigma_{LV} \qquad (21)$$

304 where the subscripts L, S, and V indicate liquid, solid, and vapor, respectively. The first term
305 on the right-hand-side of (21) denotes the kinetic energy of the flowing liquid with cross
306 sectional area of A_L. The second, third, and fourth terms denote solid-liquid, solid-vapor, and
307 liquid-vapor interfacial energies, respectively. The variable A denotes interfacial area. The
308 strategy is to compute the total system energy for each flow regime as a function of flow rate

4.1. Energy of Falling Film

When the entire fracture surface is covered with a flowing film, there is no exposed solid-vapor interface. As stated above the film is considered perfectly flat; hence, the solid-liquid and liquid-vapor areas are equal to the fracture area ($W \times L$). For a falling film with a velocity profile given by (5), the total energy equation (21) is rewritten as

$$E_f = \int_0^{h_f} W L \frac{\rho}{2} u_f(y)^2 \, \mathrm{d}y + W L (\sigma_{SL} + \sigma_{LV}) \tag{22}$$

Substituting (1) in (22) and rearranging gives the relative film energy e_f as a function of film thickness h_f, which in turn depends on the transmissivity q as given by (7):

$$e_f(q) = \frac{E_f}{WL} - \sigma_{SL} = \frac{\rho \beta^2}{15} {h_f}^5 + \sigma_{LV} \tag{23}$$

In subsequent sections, the relative film energy is compared with those of rivulets and sliding drops to identify the most likely flow regime for a given flow condition.

4.2. Energy of Straight Rivulets

During rivulet flow, the wetted and dry areas of the fracture surface are given by $L n_r w_r$ and $L d_r$, respectively (see also equations (11) and (14)). The liquid-vapor interface area is $2 L n_r R_r \theta_0$. Then, for n_r straight rivulets with velocity profiles given by (9), the total energy equation (21) is rewritten as

$$E_r = \int_{-w_r/2}^{w_r/2} \int_0^{h(x)} \frac{L n_r \rho}{2} u_r(x,y)^2 \, \mathrm{d}y \, \mathrm{d}x + L(n_r w_r \sigma_{SL} + d_r \sigma_{SV} + 2 n_r \theta_0 R_r \sigma_{LV}) \tag{24}$$

Substituting (1) in (24) and rearranging gives the relative rivulet energy e_r as a function of the transmissivity (q), the number of rivulets (n_r), and the equilibrium contact angle (θ_0):

$$e_r(q, n_r, \theta_0) = \frac{E_r}{WL} - \sigma_{SL}$$
$$= \frac{\rho \beta^2}{15} \frac{2 n_r}{W} f_2(\theta_0) R_r{}^6 + \sigma_{LV} \left\{ \frac{2 n_r}{W} R_r \left(\theta_0 - \frac{\sin 2\theta_0}{2} \right) + \cos\theta_0 \right\} \quad (25)$$

where R_r as a function of q is given by (13), and the function $f_3(\theta_0)$ is given by,

$$f_2(\theta_0) = \int_0^{\theta_0} \cos\theta \, (\cos\theta - \cos\theta_0)^5 \, d\theta$$
$$= \frac{1}{192} \left[600\theta_0 + 60\theta_0 (10\cos 2\theta_0 + \cos 4\theta_0) - 425\sin 2\theta_0 - 101\sin 4\theta_0 - \sin 6\theta_0 \right] \quad (26)$$

Note that equations (25) and (23) are similar in form. The main difference is that there are families of curves that describe the different number of rivulets and/or different contact angles. *El-Genk and Saber* [2001] provided a detailed review and verification of a slightly different form of equation (24).

4.3. Energy of sliding drops

From the geometry shown in Figure 5, the liquid-vapor, soil-liquid, and solid-vapor interface areas are given, respectively, by

$$A_{LV} = n_d \, m_d \, 2\pi R_d{}^2 (1 - \cos\theta_0) \quad (27)$$

$$A_{SL} = n_d \, m_d \, \pi R_d{}^2 \sin^2\theta_0 \quad (28)$$

$$A_{SV} = WL - A_{SL} = WL - n_d \, m_d \, \pi R^2 \sin^2\theta_0 \quad (29)$$

Because the drops travel as unit masses the kinetic energy of individual sliding drop is simply $\rho V_d \, v_d{}^2/2$. The total energy of the sliding drops is then,

$$E_d = \frac{n_d \, m_d \, \rho V_d \, v_d{}^2}{2} + A_{LV}\sigma_{LV} + A_{SL}\sigma_{SL} + A_{SV}\sigma_{SV} \quad (30)$$

Substituting (1) and (27)–(29) in (30) and simplifying it using (17) and (18) gives the relative sliding-drops energy e_d as a function of the flow rate (Q), the number of drop trains (n_d/W), the number of sliding drops per train (m_d/L), and the equilibrium contact angle (θ_0)

$$
\begin{aligned}
e_d(Q, n_d, m_d, \theta_0) &= \frac{E_d}{W L} - \sigma_{SL} \\
&= \frac{\rho L}{2W n_d m_d}\frac{Q^2}{V_d} + \sigma_{LV}\left\{\frac{n_d m_d}{WL}\left(\frac{3}{4\pi}\right)^{2/3} V_d{}^{2/3}\,\frac{\pi\left(2-2\cos\theta_0+\sin^2\theta_0\right)}{\left[\sin^4(\theta_0/2)(2+\cos\theta_0)\right]^{2/3}} + \cos\theta_0\right\}
\end{aligned}
\tag{31}
$$

where the drop volume V_d is implicitly given as a function of the flux Q by (20).

5. Constraints on Flow Regimes

In this section, we compare the relative energies of different flow regimes and designate the regime with lowest energy as the most likely one for the given flow conditions. As indicated by the relative energy equations, the total energy is the sum of the kinetic and interfacial energies. What determines the most likely (stable) flow regime at a given flow condition is the relative importance of these components.

For all subsequent illustrative calculations, we consider a set of liquid properties and solid-liquid contact angles that reasonably approximate a natural fracture-water system. The properties are listed in Table 1.

5.1. Sliding Drop Regime

The relative energy curves of sliding drops (31) traveling along a single train $(n_d = 1)$ for $m_d = 1, 2, 3, \text{and } 4$ are plotted in Figure 7a. At the lowest flow rate range, a single sliding drop (per unit fracture length) has the lowest relative energy and is thus the most likely flow mechanism. At a flow rate of approximately $0.002\times10^{-6}\,\text{m}^3\,\text{sec}^{-1}\,\text{m}^{-1}$, the energy curves of

363 $m_d = 1$ and $m_d = 2$ intersect; beyond the intersection flow rate, the two-drop condition has
364 lowest energy. This implies, given a fixed flow rate, that two drops with larger liquid-vapor
365 surface area (hence, more interfacial potential energy) travel at a much slower speed (hence,
366 lower kinetic energy) such that the total energy of the two-drop configuration is lower than that
367 of the one-drop regime. Similar transitions from $m_d = 2$ to $m_d = 3$ and $m_d = 3$ and $m_d = 4$ are
368 shown in Figure 7a. The transitions from m_d to $m_d + 1$ are illustrated in Figure 7b as a function
369 of flow rate. The exact transition from m_d to $m_d + 1$ occurs when the respective relative energies
370 (31) are identical, that is,

371 $$e_d\left(Q_{dd}, n_d, m_d, \theta_0\right) = e_d\left(Q_{dd}, n_d, m_d + 1, \theta_0\right) \tag{32}$$

372 where Q_{dd} denotes the critical flow rate at which the transition from m_d to $m_d + 1$ occurs.
373 Collecting like-terms in (32) and simplifying yields

374 $$\frac{Q_{dd}\, L}{n_d}\frac{\rho}{2W}\left(\frac{1}{m_d\, V_d\left(m_d\right)} - \frac{1}{\left(m_d + 1\right)V_d\left(m_d + 1\right)}\right) + \frac{\Theta\, L}{n_d}\left(\frac{1}{V_d\left(m_d\right)} - \frac{1}{V_d\left(m_d + 1\right)}\right) = \frac{\Theta}{Q}\frac{\sigma_{LV}}{\mu}\Delta\theta \tag{33}$$

375 where

376 $$\Theta = \sigma_{LV}\frac{n_d}{WL}\left(\frac{3}{4\pi}\right)^{2/3}\frac{1}{\gamma\beta}\frac{\pi\left(2 - 2\cos\theta_0 + \sin^2\theta_0\right)}{\left[\sin^4\left(\theta_0/2\right)\left(2 + \cos\theta_0\right)\right]^{2/3}}$$

377 Equation (33) was evaluated numerically and its values for the first few number of sliding
378 droplets are shown in Figure 7b by circular symbols.

379 Figure 7. (a) Relative energy curves as functions of flow rate for 1, 2, 3, and 4
380 sliding drops and (b) the corresponding number of drops satisfying the
381 minimum-energy configuration.

5.2. Transition from Sliding-Drops to Straight-Rivulet Flow Regime

In Figure 8a, the relative energy of sliding drops (32) for $m_d =$ 1, 5, 10, 20, 50, 100 and 120, and the relative energy (25) of one rivulet ($n_r = 1$) are plotted over a wide range of flow rates (Q). As the flow rate is increased, the number of drops sliding along a given train linearly increases; accordingly, the distance between the centers of two successive drops (L/m_d) decreases. When the drops begin to touch, a straight laminar rivulet is formed [*Schmuki and Laso*, 1990]. From the spherical cap approximation, this critical transition occurs when the drop diameter is equal to the inter-drop distance. The critical flow rate at which the transition from drop regime to rivulet regime (Q_{dr}) occurs is implicitly given by

$$\frac{L}{m_d} = 2\, R_d\left(Q_{dr}\right)\sin\theta_0 \tag{34}$$

where R_d is the radius of the spherical-cap drop as given by (17). In Figure 8b, the number of drops as a function flow rate (33) and the critical condition (34) are plotted as a solid line and a black dot, respectively. The intersection of the two curves, marked by a circular symbol, denotes the transition from sliding drop regime to straight rivulet regime.

Figure 8. (a) Relative energy curves as functions of flow rate for several numbers of sliding drops along one train and (b) the corresponding number of drops satisfying the minimum-energy configuration.

In Figure 9, we show the m_d to $m_d + 1$ transitions for a number of contact angles, as well as the envelope for droplet regime to rivulet regime transitions. At smaller contact angles, the drops are likely to leave a trail of thin film behind them [*Bico and Quere*, 2000] and the mechanism of transition from drop regime to rivulet regime described in this subsection is likely

403 to overestimate the number of drops at this transition. This error is expected to be exacerbated by
404 the fact that the flow rate at the transition is much smaller in small contact angles.

405 Figure 9. Number of sliding drops in one train as a function of flow rate for
406 several contact angles. The shaded region denotes rivulet flow regime.

407 **5.3. Rivulet flow regime**

408 We start by considering relative energies of a few rivulets e_r. In Figure 10a, (25)
409 (relative energy) is plotted for one, two, three and four-rivulet scenarios (n_r = 1, 2, 3 and 4,
410 respectively) as a function of flow rate (Q). At low flow rate a single rivulet has the lowest
411 energy and is thus the most likely flow mechanism. At a flow rate of approximately
412 $0.25\times10^{-6}\,\mathrm{m}^3\,\mathrm{sec}^{-1}\,\mathrm{m}^{-1}$, the energy curves for one- and two-rivulet conditions intersect. When
413 the flow rate is increased beyond this critical value, the contribution of the kinetic energy gain to
414 the single-rivulet system is more significant compared to the two-rivulet system, which has
415 larger liquid-vapor interface area but smaller velocity. Hence, the two-rivulet system becomes
416 the more stable (preferable) configuration. Similar transitions to higher number of rivulets occur
417 at higher flow rates; the first few transitions are shown in Figure 10b. The exact transition from
418 n_r to n_r+1 occurs when the respective relative energies (25) are identical,

419 $$e_r(Q_{rr}, n_r, \theta_0) = e_r(Q_{rr}, n_r+1, \theta_0) \tag{35}$$

420 where Q_{rr} is the critical flow rate at which transition from n_r to n_r+1 takes place. Solving (35)
421 for Q_{rr} and algebraic manipulation gives,

422 $$Q_{rr}(n_r, \theta_0) = \left(\frac{2\beta}{3}\right)^{1/5} f_1(\theta_0)\left\{\frac{5}{f_2(\theta_0)}\frac{\sigma_{LV}}{\rho\beta}(2\theta-\sin 2\theta)\sqrt{n_r(1+n_r)}\,\frac{(1+n_r)^{3/4}-n_r^{3/4}}{(1+n_r)^{1/2}-n_r^{1/2}}\right\}^{4/5} \tag{36}$$

Equation (36) is plotted in Figure 10b for $n_r = 1, 2, \text{and } 3$ as the circle symbols. We further note that

$$\sqrt{n_r(1+n_r)}\,\frac{(1+n_r)^{3/4} - {n_r}^{3/4}}{(1+n_r)^{1/2} - {n_r}^{1/2}} \approx \frac{3}{2}\left(n_r + \frac{1}{2}\right)^{5/4} \tag{37}$$

The maximum error introduced by (37) is 7% for $n_r = 1$; it is less than 1% for $n_r > 3$ and less than 0.1% for $n_r > 11$. By substituting (37) in (36), and rearranging we obtain

$$n_{rr} = -1/2 + A_0\, Q_{rr} \tag{38}$$

where n_{rr} denotes the transition from n_r to $n_r + 1$, and the coefficient A_0 is

$$A_0 = (3/2)^{1/5}(2/15)^{4/5}\beta^{3/5}(\rho/\sigma_{LV})^{4/5}\left\{\frac{f_2(\theta_0)}{(2\theta - \sin 2\theta)\, f_1(\theta_0)^{5/4}}\right\}^{4/5} \tag{39}$$

Equation (38) indicates that the optimal number of rivulets n_{rr} is linearly related to the flux Q_{rr}. Furthermore, the slope of the relationship is a function of the contact angle θ_0 and the liquid properties.

Figure 10.(a) Relative energy curves as a function of flow rate for 1, 2, 3 and 4 parallel rivulets, and (b) the corresponding number of rivulets satisfying the minimum-energy configuration

5.4. Transition from Rivulet Flow Regime to Film Flow Regime

In Figure 11a, the relative energy of straights rivulets (25) for n_r = 1, 5, 10, 50, 100, 150 and 200, and the relative energy of stable film (23) are plotted over a wider range of flow rate (Q). The n_r to $n_r + 1$ transitions (36) are plotted as a function of the critical flow rate Q_{rr} in Figure 11b. Notice in Figure 11a that the rivulet energy curves, up to approximately n_r = 100, cross the film energy curve at progressively increasing flow rates. Moreover, notice that within

443 this flow-rate range, all the transitions from n_r to n_r+1 occur while the rivulet energies are
444 below that of the film; therefore the stable flow regime is rivulet flow. Beyond this critical flow
445 rate, all the n_r to n_r+1 transitions occur while the rivulet energies are higher than the film
446 energy. In the following, we derive expressions for the critical flow rate at which a stable film
447 breaks apart into multiple rivulets, and calculate the corresponding maximum number of rivulets.
448 First, the flow rate at which the rivulet energy curve with an arbitrary n_r intersects the film
449 energy curve, $e_r(Q,n_r,\theta_0)=e_f(Q)$, is obtained by equating (23) and (25) and factoring out Q
450 and n_r:

451 $$A_1 Q^{5/3} + A_2 n_r^{-1/2} Q^{3/2} + A_3 n_r^{3/4} Q^{1/4} + A_4 = 0 \tag{40}$$

452 where

453 $$A_1 = -\frac{3^{2/3}}{5}\beta^2\rho(W\beta)^{-5/3}$$

454 $$A_2 = \frac{\sqrt{3/2}}{5W}\beta^2\rho\, f_2(\theta_0)\cdot(f_1(\theta_0)\beta)^{-3/2}$$

455 $$A_3 = \frac{2^{3/4}\,3^{1/4}}{W}\sigma_{LV}\cdot\left(\theta_0 - \frac{\sin 2\theta_0}{2}\right)(f_1(\theta_0)\beta)^{-1/4}$$

456 $$A_4 = \sigma_{LV}\cdot(1-\cos\theta_0)$$

457 Figure 11.(a) Relative energy curves as a function of flow rate for several
458 numbers of parallel rivulets and a stable film, and (b) the corresponding
459 number of rivulets satisfying the minimum-energy configuration.

460 The condition for the transition from rivulet flow regime to film flow regime requires
461 finding the largest n_r to n_r+1 transition that satisfies $e_r(Q,n_r,\theta_0)\le e_f(Q)$. Thus a substituting
462 (38) in (40) we obtain

463 $$A_1 Q_{rf}^{5/3} + A_2 \left(A_0 Q_{rf} - 1/2\right)^{-1/2} Q_{rf}^{3/2} + A_3 \left(A_0 Q_{rf} - 1/2\right)^{3/4} Q_{rf}^{1/4} + A_4 = 0 \qquad (41)$$

464 where Q_{rf} stands for the critical flow rate at the transition from film flow to rivulet flow regime
465 (or vise versa). Note that (41) has to be evaluated numerically to obtain Q_{rf} as a function of the
466 fluid and contact angle. In Figure 11b, Q_{rf} was calculated for the standard liquid and contact
467 angle using (41) and the respective n_{rf} was obtained from (38). This transition point from rivulet
468 flow to film flow is designated by a black dot. To highlight the importance of contact angle in
469 the break up of film to rivulets and the transitions within the rivulet flow regime the n_r to n_r+1
470 transitions (38) are plotted in Figure 12 for a number of contact angles. An envelope marking the
471 transition from rivulet regime to film regime is also shown (equations (41) and (38)). The two
472 important results of this plot are (1) the critical flow rate at which a stable film breaks up to
473 rivulets increases with increasing contact angle, and (2) the maximum number of rivulets at this
474 breakdown increases with increaseing contact angle.

475 Figure 12.Number of rivulets as a function of flow rate for several contact angles.
476 The shaded region denotes film flow.

477 **5.5. Instability of the Film Flow Regime**

478 The Nusselt's film flow equation assumes that the film surface is free of any ripples and
479 waves. This assumption works only under low to intermediate Reynolds number. *Patnaik and*

480 *Perez-Blanco* [1996] provided classification of the film flow regime based on stability. Their
481 classification depends on the Reynolds number:

482 $$Re_S \equiv 4Re = \frac{4Q\rho}{W\mu} \tag{42}$$

483 The Nusselt's film flow typically occurs in the $Re_S \le 20$ range. Films with high-
484 frequency low-amplitude capillary waves occur in the range $20 < Re_S < 200$. These capillary
485 waves originate when variations in surface tension caused by localized temperature and
486 concentration gradients are comparable to the gravity and viscous forces. However, "statistical
487 analysis shows that the mean film thickness for wavy film is close to the stable state value for
488 flat films when the film is thin (i.e., low Reynolds numbers)" [*Dragila*, 1999]. Thus, we regard
489 the Nusselt's approximation to hold for $Re_S \le 200$.

490 For $Re_S > 200$, the main cause of the perturbation is an inertial force. The resulting waves
491 can be laminar ($200 < Re_S < 1000$) or turbulent ($1000 < Re_S < 4000$). These waves roll over the
492 substrate film at a much higher velocity than the substrate. The flat film surface solutions no
493 longer apply in this range. When $Re_S > 4000$, the flow is fully turbulent. The unstable flows at
494 very high flow rates (on the order of $Re_S \ge 1000$) are considered to be beyond the interest of
495 hydrological applications.

496 6. Summary and Conclusions

497 Using simplified flow geometries and assuming laminar flow, we derived energy
498 equations for the major flow regimes that are likely to occur in fractured systems. The energy
499 equations were used to provide constraints on the flow rates that allowed us to delineate the flow
500 regimes. The potential implications of the results presented in this paper become apparent when

looking at all the transitions over wide ranges of flow rate and wettability of the fracture surface. The transitions from drop sliding regime to rivulet regime, from rivulet regime to stable film regime, and onset of waviness and turbulence on films are shown by plotting equations (34) and (41) and instability conditions specified in subsection 5.5 (see Figure 13). The flow rate spectrum in Figure 13 covers several orders of magnitude, and the contact angles range from slightly hydrophobic ($\theta_0 \approx 0°$) to moderately hydrophobic ($\theta_0 \approx 90°$). These results depict the boundaries between flow regimes for a vertical fracture. According to Figure 13, steady flow (stable film and rivulets) occurs only in the intermediate flow rate range. Outside of this region, a steady and constant input flux yields an episodic flow downstream. At lower flow rates, episodicity emanates from disintegration of rivulets into trains of sliding drops. At higher flow rates, destabilization of films by surface waves is responsible for episodic flows.

As shown in Figure 13, an elevated contact angle (reduced wettability) broadens the range of the steady flow regimes. At high contact angles, the weak adhesion of liquids onto the fracture surfaces decreases the tendency for rivulets to breakup into drops, as shown by the rapid decrease of the flux at which transition from sliding drops to rivulet regime occurs.

The flux at which transition from rivulet regime to stable film flow occurs increases with contact angle. This is because the ratio of the rivulet cross-sectional area to its liquid-vapor interface area decreases with contact angle (see Figure 4), allowing the rivulets to transport liquid at higher flow rates but lower potential energy compared to films. At a contact angle of $\theta_0 \approx 45°$, the possibility for stable films to form on vertical fractures is eliminated. Note that for fracture inclination angles other than vertical, the curves in Figure 13 are expected shift; nevertheless, the general trend remains the same.

Figure 13. Summary of dominant flow regimes for wide ranges of contact angle and flow rate.

The main conclusions drawn from this study are:

1. A single flow mechanism (hence, single conceptual model of flow) is not adequate to describe flow in unsaturated fractures. Dissimilar flow regimes can coexist in a fractured rock, if the rock comprises fractures with different inclination angles and/or wettability. Thus, a realistic self-consistent flow model should be able to discern and apply the appropriate conceptual model fitting for any given flow condition.

2. The implications of assuming a wrong flow regime are far reaching. For example, the fracture-matrix interaction is less significant in a rivulet regime compared to films. In addition, particles in rivulets travel at much slower velocity than in films (under identical volumetric flux per cross section). The consequences of these differences to solute diffusion and/or travel time are apparent.

3. Episodic flow initiated in any one given fracture has the potential of cascading to downstream fractures that feed off the outflow from the given fracture. Only a few initiators are adequate to produce highly erratic flow from a seemingly steady source flux (see Or and Ghezzehei, in preparation).

The potential applications of our results are evident from the introduction. However, further experimental investigations will be needed to provide realistic model parameters and to test the proposed constraints.

References

Adamson, A.W., and A.P. Gast, *Physical chemistry of surfaces*, John Wiley and Sons, Inc., New York, New York, 1997.

Allen, R.F., and C.M. Biggin, Longitudinal flow of a lenticular liquid filament down an inclined plane, *Physics of Fluids*, *17* (2), 287-291, 1974.

Amundsen, H., G. Wagner, U. Oxaal, P. Meakin, J. Feder, and T. Jossang, Slow two-phase flow in artificial fractures: Experiments and simulations, *Water Resources Research*, *35* (9), 2619-2626, 1999.

Bankoff, S.G., Minimum thickness of a draining liquid film, *International Journal of Heat and Mass Transfer*, *14* (12), 2143-&, 1971.

Bankoff, S.G., Problems in interfacial instability, *Annals of the New York Academy of Sciences*, *404* (MAY), 405-419, 1983.

Benson, D.A., A model of water streaking down a wall, *Water Resources Research*, *37* (2), 427-430, 2001.

Berbente, C.P., and E. Ruckenst, Hydrodynamics of wave flow, *AIChE Journal*, *14* (5), 772-&, 1968.

Berkowitz, B., Characterizing flow and transport in fractured geological media: A review, *Advances in Water Resources*, *25* (8-12), 861-884, 2002.

Bertels, S.P., D.A. DiCarlo, and M.J. Blunt, Measurement of aperture distribution, capillary pressure, relative permeability, and in situ saturation in a rock fracture using computed tomography scanning, *Water Resources Research*, *37* (3), 649-662, 2001.

Bico, J., and D. Quere, Liquid trains in a tube, *Europhysics Letters*, *51* (5), 546-550, 2000.

565 Brauner, N., Modelling of wavy flow in turbulent free falling films, *International Journal of*
566 *Multiphase Flow, 15* (4), 505-520, 1989.
567 Cassie, A.B.D., Contact angles, *Discussions of the Faraday Society, 3*, 11-16, 1948.
568 Detwiler, R.L., H. Rajaram, and R.J. Glass, Experimental and simulated solute transport in a
569 partially-saturated, variable-aperture fracture - art. No. 1272, *Geophysical Research Letters*,
570 *29* (8), 1272, 2002.
571 Dobson, P.F., T.J. Kneafsey, J. Hulen, and A. Simmons, Porosity, permeability, and fluid flow in
572 the yellowstone geothermal system, wyoming, *Journal of Volcanology and Geothermal*
573 *Research, 123* (3-4), 313-324, 2003.
574 Doe, T.W., What do drops do? Surface wetting and network geometry effects on vadose-zone
575 fracture flow, in *Conceptual models of flow and transport in the fractured vadose zone*,
576 edited by National Academy of Sciences, pp. 243-270, National Academy Press,
577 Washington, DC, 2001.
578 Dragila, M.I., A new theory for transport in unsaturated fractures: Free-surface film flows, Ph.D.
579 thesis, University of Nevada, Reno, 1999.
580 Dragila, M.I., and N. Weisbrod, Parameters affecting maximum fluid transport in large aperture
581 fractures, *Advances in Water Resources, 26* (12 SU -), 1219-1228, 2003.
582 Dragila, M.I., and S.W. Wheatcraft, Free-surface films, in *Conceptual models of flow and*
583 *transport in the fractured vadose zone*, edited by N.A.o.S. Panel on Conceptual Models of
584 Flow and Transport in the Fractured Vadose Zone, pp. 217-242, National Academy Press,
585 Washington, DC, 2001.
586 El-Genk, M.S., and H.H. Saber, Minimum thickness of a flowing down liquid film on a vertical
587 surface, *International Journal of Heat and Mass Transfer, 44* (15), 2809-2825, 2001.

588 Fourar, M., S. Bories, R. Lenormand, and P. Persoff, 2-phase flow in smooth and rough fractures
589 - measurement and correlation by porous-medium and pipe flow models, *Water Resources*
590 *Research*, *29* (11), 3699-3708, 1993.
591 Glass, R.J., and M.J. Nicholl, Physics of gravity fingering of immiscible fluids within porous
592 media - an overview of current understanding and selected complicating factors, *Geoderma*,
593 *70* (2-4), 133-163, 1996.
594 Glass, R.J., M.J. Nicholl, A.L. Ramirez, and W.D. Daily, Liquid phase structure within an
595 unsaturated fracture network beneath a surface infiltration event: Field experiment - art. No.
596 1199, *Water Resources Research*, *38* (10), 1199, 2002.
597 Hakami, E., and E. Larsson, Aperture measurements and flow experiments on a single natural
598 fracture, *International Journal of Rock Mechanics & Mining Sciences & Geomechanics*
599 *Abstracts*, *33* (4), 395-404, 1996.
600 Hobler, T., Minimum surface wetting (polish), *Chemia Stosowana*, *2B*, 145-159, 1964.
601 Hughes, D.T., and T.R. Bott, Minimum thickness of a liquid film flowing down a vertical tube,
602 *International Journal of Heat and Mass Transfer*, *41* (2), 253-260, 1998.
603 Jayanti, S., and G.F. Hewitt, Hydrodynamics and heat transfer of wavy thin film flow,
604 *International Journal of Heat and Mass Transfer*, *40* (1), 179-190, 1997.
605 Joo, S.W., S.H. Davis, and S.G. Bankoff, A mechanism for rivulet formation in heated falling
606 films, *Journal of Fluid Mechanics*, *321*, 279-298, 1996.
607 Kim, H.-Y., H.J. Lee, and B.H. Kang, Sliding of liquid drops down an inclined solid surface,
608 *Journal of Colloid and Interface Science*, *247* (2), 372-380, 2002.
609 Kneafsey, T.J., and K. Pruess, Laboratory experiments on heat-driven two-phase flows in natural
610 and artificial rock fractures, *Water Resources Research*, *34* (12), 3349-3367, 1998.

Lee, J., Kapitzas method of film flow description, *Chemical Engineering Science*, *24* (8), 1309-&, 1969.

Mikielewicz, J., and J.R. Moszynski, Minimum thickness of a liquid-film flowing vertically down a solid-surface, *International Journal of Heat and Mass Transfer*, *19* (7), 771-776, 1976.

National Academy of Sciences, *Rock fractures and fluid flow: Contemporary understanding and applications*, National Academy Press, Washington, D.C., 1996.

Nicholl, M.J., R.J. Glass, and S.W. Wheatcraft, Gravity-driven infiltration instability in initially dry nonhorizontal fractures, *Water Resources Research*, *30* (9), 2533-2546, 1994.

Or, D., and M. Tuller, Flow in unsaturated fractured porous media: Hydraulic conductivity of rough surfaces, *Water Resources Research*, *36* (5), 1165-1177, 2000.

Patnaik, V., and H. Perez-Blanco, Roll waves in falling films: An approximate treatment of the velocity field, *International Journal of Heat and Fluid Flow*, *17* (1), 63-70, 1996.

Penev, V., Boyadjie.C, Vorotili.Vp, and V.S. Krylov, Wavy flow of thin liquid films, *International Journal of Heat and Mass Transfer*, *15* (7), 1395-&, 1972.

Persoff, P., and K. Pruess, Two-phase flow visualization and relative permeability measurement in natural rough-walled rock fractures, *Water Resources Research*, *31* (5), 1175-1186, 1995.

Podgorski, T., J.M. Flesselles, and L. Limat, Corners, cusps, and pearls in running drops - art. No. 036102, *Physical Review Letters*, *8703* (3), 6102-NIL_95, 2001.

Ponter, A.B., and K.M. Aswald, Minimum thickness of a liquid-film flowing down a vertical surface - validity of mikielewicz and moszynskis equation, *International Journal of Heat and Mass Transfer*, *20* (5), 575-576, 1977.

633 Pruess, K., A mechanistic model for water seepage through thick unsaturated zones in fractured
634 rocks of low matrix permeability, *Water Resources Research, 35* (4), 1039-1051, 1999.
635 Schmuki, P., and M. Laso, On the stability of rivulet flow, *Journal of Fluid Mechanics, 215*,
636 125-143, 1990.
637 Soo, S.L., Instability in a falling liquid film, *International Journal of Heat and Fluid Flow, 17*
638 (5), 526-527, 1996.
639 Su, G.W., J.T. Geller, K. Pruess, and J.R. Hunt, Solute transport along preferential flow paths in
640 unsaturated fractures, *Water Resources Research, 37* (10), 2481-2491, 2001.
641 Su, G.W., J.T. Geller, K. Pruess, and F. Wen, Experimental studies of water seepage and
642 intermittent flow in unsaturated, rough-walled fractures, *Water Resources Research, 35* (4),
643 1019-1037, 1999.
644 Tokunaga, T.K., and J.M. Wan, Water film flow along fracture surfaces of porous rock, *Water*
645 *Resources Research, 33* (6), 1287-1295, 1997.
646 Tokunaga, T.K., and J.M. Wan, Surface-zone flow along unsaturated rock fractures, *Water*
647 *Resources Research, 37* (2), 287-296, 2001.
648 Tokunaga, T.K., J.M. Wan, and S.R. Sutton, Transient film flow on rough fracture surfaces,
649 *Water Resources Research, 36* (7), 1737-1746, 2000.
650 Towell, G.D., and L.B. Rothfeld, Hydrodynamics of rivulet flow, *Aiche Journal, 12* (5), 972-&,
651 1966.
652 Tuller, M., D. Or, and L.M. Dudley, Adsorption and capillary condensation in porous media:
653 Liquid retention and interfacial configurations in angular pores, *Water Resources Research,*
654 *35* (7), 1949-1964, 1999.

Yih, C.S., Stability of liquid flow down an inclined plane, *Physics of Fluids*, *6* (3), 321-334, 1963.

Zhong, L.R., A. Mayer, and R.J. Glass, Visualization of surfactant-enhanced nonaqueous phase liquid mobilization and solubilization in a two-dimensional micromodel, *Water Resources Research*, *37* (3), 523-537, 2001.

List of Tables

Table 1. Properties of liquids used by [*Kim et al.*, 2002] and fitted empirical constants

	Liquid Properties			Fitted Constants		
Liquid	ρ [kg m^{-3}]	μ [Pa s]	σ_{LV} [N m^{-1}]	θ_0 [rad]	γ	$\Delta\theta$
Ethylene glycol	1114	0.0209	0.0484	1.225	0.0015	0.0004
Glycerin (80 wt%) water (20 wt%)	1228	0.0600	0.0641	1.285	0.0020	0.0009
Glycerin	1260	0.95	0.063	1.363	0.0016	0.0006
Water†	998.2	0.00102	0.0727	$\pi/9$	0.003‡	0.001‡

† Water was not used in the experiments of *Kim et al*. [2002].

‡ These values were used for water on rock surface in the illustrative examples.

List of Figures

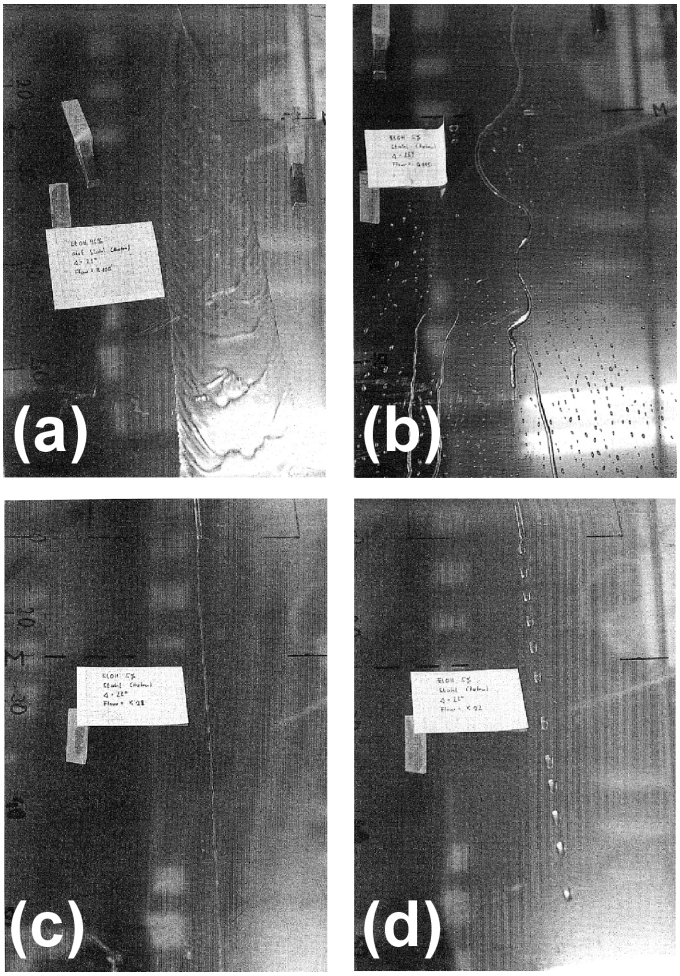

Figure 1. Photos of different flow regimes from experiments conducted by Schmuki and Laso [1990] (a) wavy film flow, (b) meandering rivulets, (c) straight rivulet, and (d) sliding drops. (Permission to reprint will be requested).

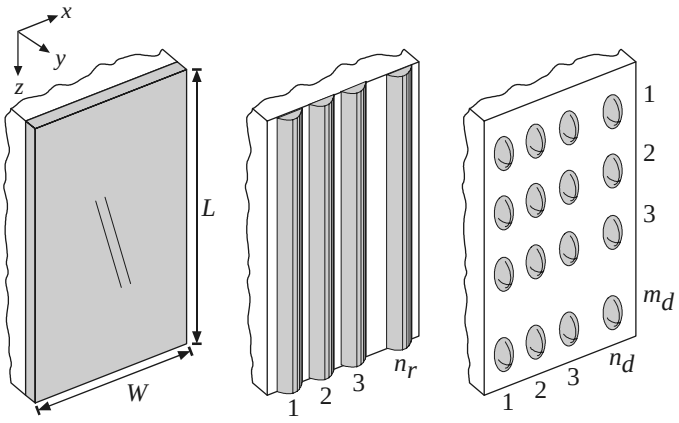

(a) Falling film (b) Straight rivulets (c) Sliding drops

Figure 2. Conceptual geometries of flow regimes used in this study.

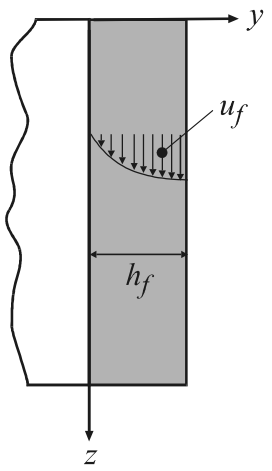

Figure 3. Schematic representation of a falling film and its velocity profile.

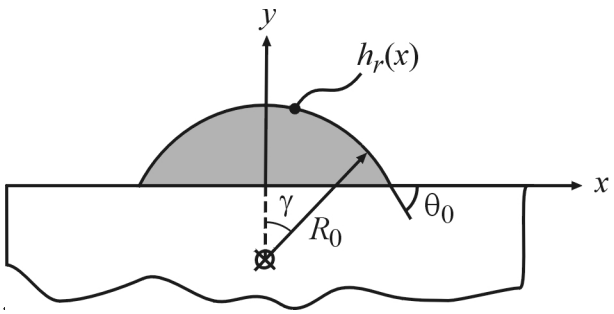

Figure 4. Schematic representation of the cross-section of a straight rivulet.

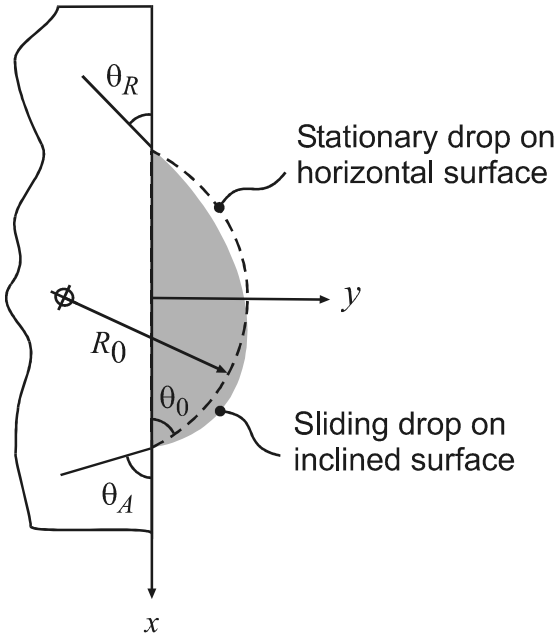

Figure 5. Definition of variables representing a sliding drop.

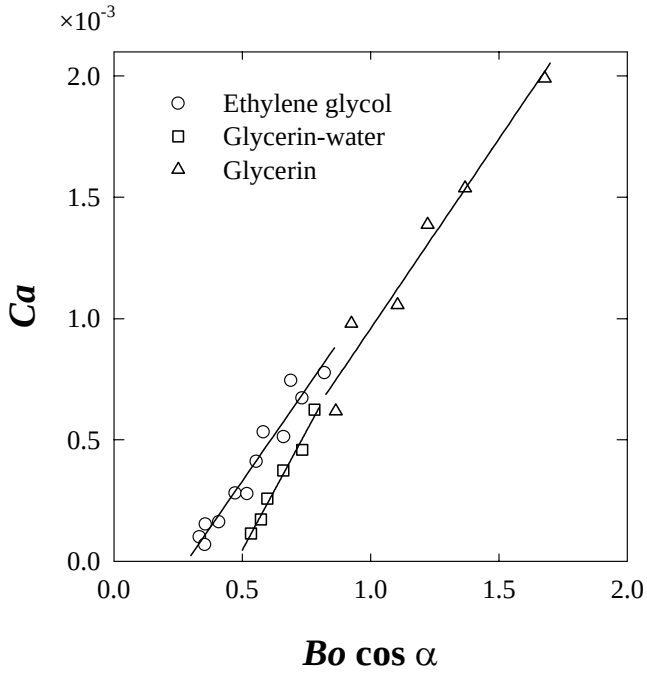

Figure 6. Relationship between Capillary number and Bond number for sliding drops of different liquids on smooth polycarbonate surface [Kim et al., 2002] and fitted scaling law given by (16).

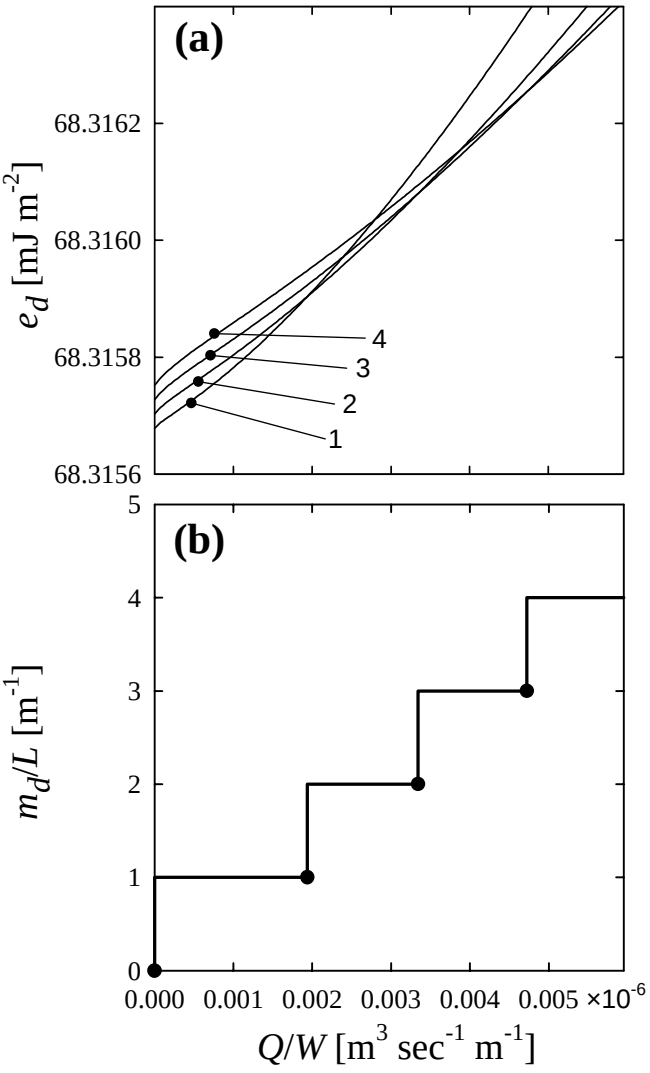

Figure 7. (a) Relative energy curves as functions of flow rate for 1, 2, 3, and 4 sliding drops and (b) the corresponding number of drops satisfying the minimum-energy configuration.

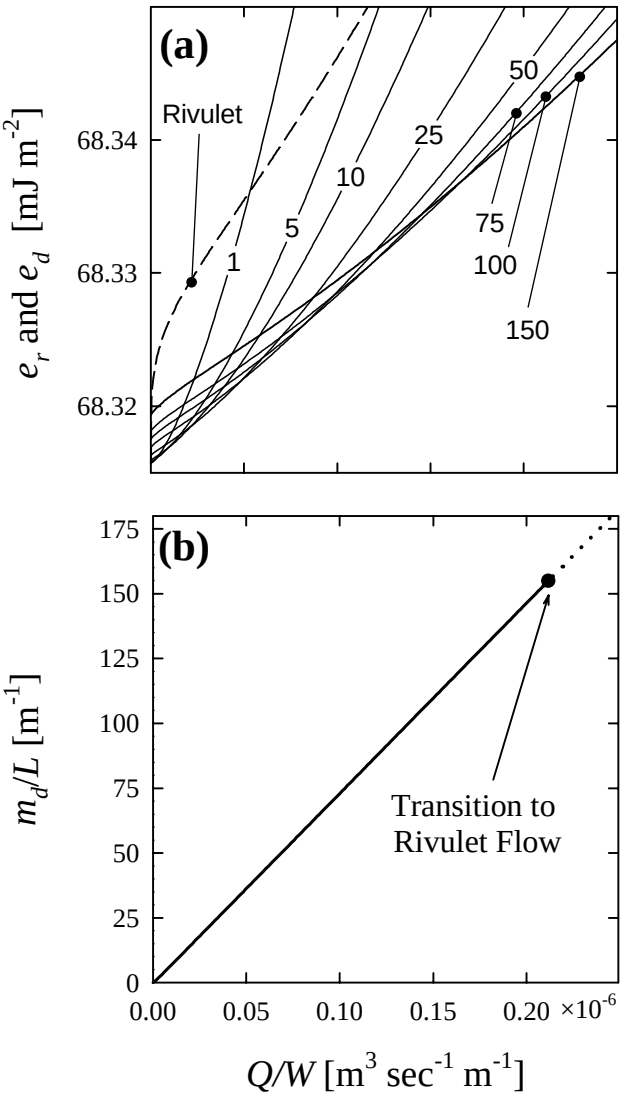

Figure 8. (a) Relative energy curves as functions of flow rate for several numbers of sliding drops along one train and (b) the corresponding number of drops satisfying the minimum-energy configuration.

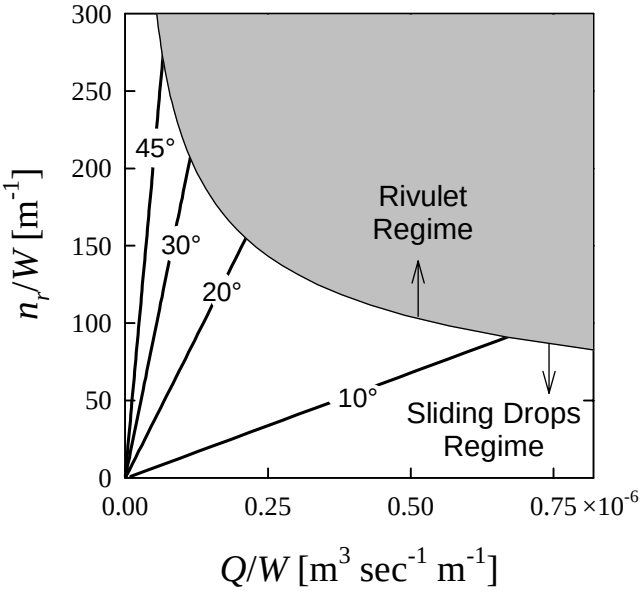

Figure 9. Number of sliding drops in one train as a function of flow rate for several contact angles. The shaded region denotes rivulet flow regime.

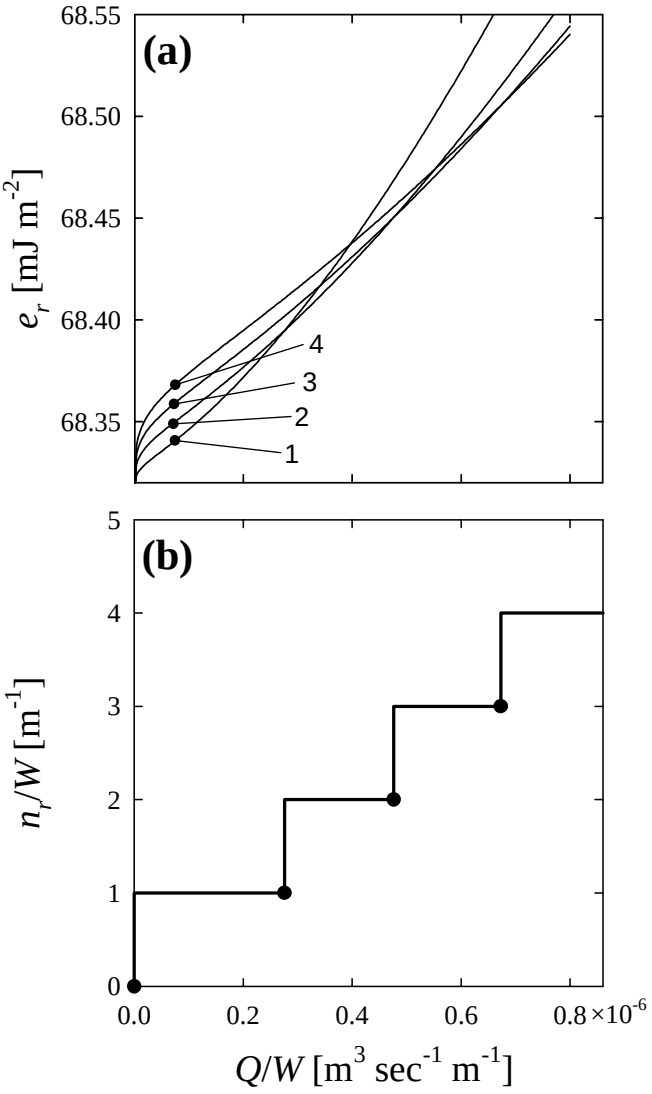

Figure 10. (a) Relative energy curves as a function of flow rate for 1, 2, 3 and 4 parallel rivulets, and (b) the corresponding number of rivulets satisfying the minimum-energy configuration

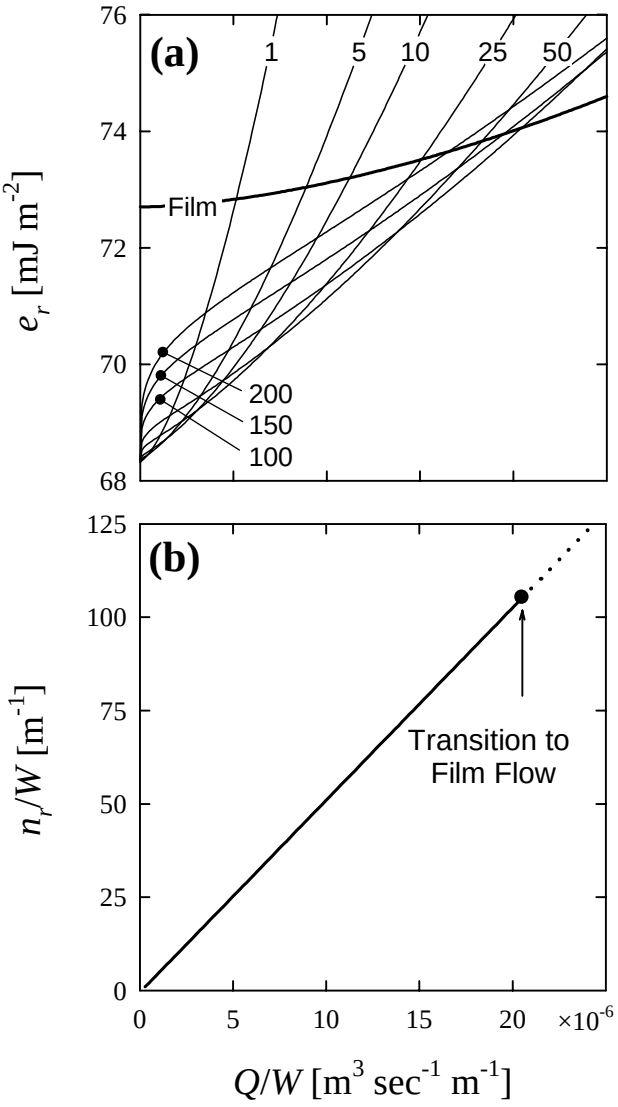

Figure 11. (a) Relative energy curves as a function of flow rate for several numbers of parallel rivulets and a stable film, and (b) the corresponding number of rivulets satisfying the minimum-energy configuration.

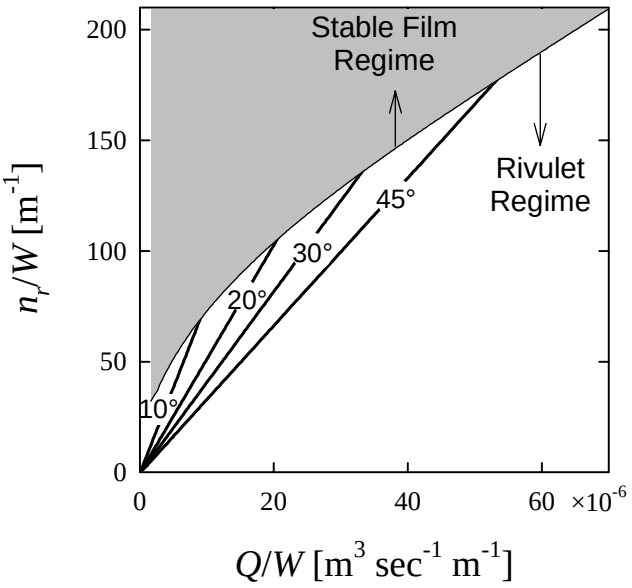

Figure 12. Number of rivulets as a function of flow rate for several contact angles. The shaded region denotes film flow.

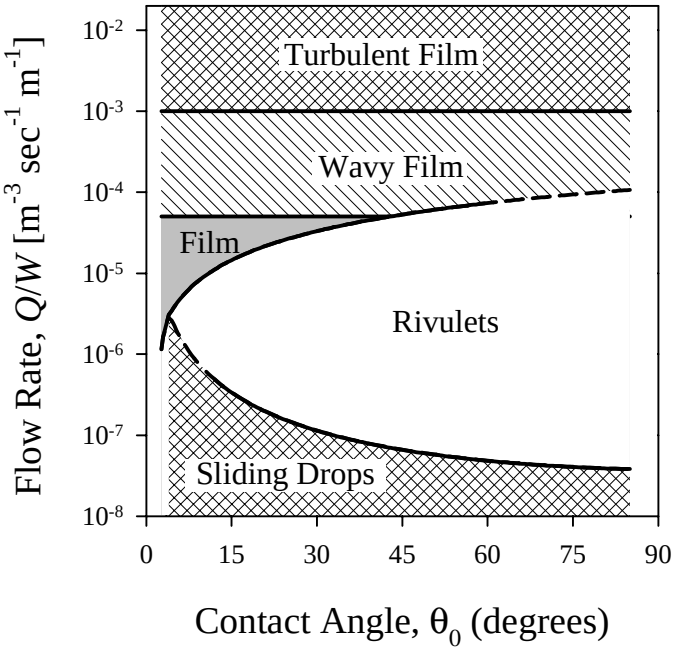

Figure 13. Summary of dominant flow regimes for wide ranges of contact angle and flow rate.